

# **COGEAR**

## **MODULE 3:**

### **Geotechnical investigations at the instrument borehole sites**

**Del. No.: 3b.2.3.1**

**Authors: Moore, J., Gischig, V., Button, E.,  
and Löw, S.**

**Engineering Geology, ETH Zürich**

March 8, 2010

### Task 3b.2.3

## Geotechnical investigations at the instrument borehole sites

### Deliverable: 3b.2.3.1

Jeffrey Moore, Valentin Gischig, Edward Button, and Simon Loew

Engineering Geology, ETH Zurich

### Summary

This report summarizes research activities conducted at the COGEAR instrumented borehole site at the Randa rock slope instability. Major outcomes and surveys performed are described, detailed borehole logs are presented, and the interested reader is directed to relevant literature for a complete discussion of results and additional information. Other relevant information regarding the Randa borehole site is described in deliverable 3b.2.2.1: Geotechnical Measurements in the Matter Valley. Geological / geotechnical investigations in the area of the proposed Graechen borehole site will be reported later in the thesis of Heynen (2010).

### Randa rockslide

In April and May of 1991, two consecutive rockslides occurred from a cliff high above the village of Randa in the Matter Valley of Switzerland (Figures 1 and 2). These complex rockslides released a cumulative volume of approximately 30 million m<sup>3</sup> of crystalline rock, with each of the rockslide stages occurring over several hours (Schindler et al., 1993). Slide debris buried important transportation lines including the road and railway leading to Zermatt, and dammed the Matternvispa River which flooded a portion of the upstream town of Randa. No fatalities resulted from either rockslide event.

The Randa rockslide has been the subject of intensive research since its failure in 1991 (e.g. Schindler et al., 1993; Sartori et al., 2003; Eberhardt et al., 2004; Heincke, 2006a,b; Loew et al., 2007; Spillmann et al., 2007a,b; Willenberg et al., 2008a,b). Around 5 million m<sup>3</sup> of rock above and behind the scarp of the 1991 rockslides remains unstable today, moving towards the valley at rates up to 20 mm/yr (Gischig et al., 2009). In 2002, an "in-situ laboratory" was created at Randa with goal of supporting multi-disciplinary research on the rockslide structure and kinematics, and investigations into the mechanics and driving forces of the currently unstable rock mass. These studies have employed a wide range of methods, including passive and active seismics, borehole and surface geo-radar, helicopter-based LiDAR, ground-based DInSAR, local and regional geodetic surveying, and traditional and advanced in-situ monitoring techniques.

### Geological and geophysical characterization of rock mass structure

Extensive geological mapping and geophysical experiments were performed at the Randa site, which focused on characterization of the internal structure of the unstable rock mass. The following techniques were used to construct a 3D model of the instability (Willenberg et al., 2008a):

- Geological mapping (Willenberg, 2004; Willenberg et al., 2008a)
- 3D seismic refraction tomography (Heincke, 2005; Heincke et al., 2006a)
- 3D surface and borehole geo-radar (Heincke et al., 2006b; Spillmann et al., 2007b)

The primary lithologies identified can be grouped into two categories – orthogneiss and paragneiss. The orthogneiss is a competent quartz-rich augengneiss, termed the Randa augengneiss, while the paragneiss is fine grained, contains more micaceous minerals, and is interbedded with chloritic schists (Figure 3). Detailed surface and borehole televiewer mapping revealed that foliation of these gneisses dips primarily to the west, into the slope. Several fracture sets cut the foliation and break the rock mass into blocks. Two scales of discontinuity networks were recognized: a small-scale network consisting of fractures with lengths of up to 5 m, and a large-scale network of faults and fracture zones. The large-scale fracture network includes fracture zones, brittle faults and brittle-ductile shear zones that dip either parallel to foliation to the W or steeply inclined to the E and NW. Similar to the small-scale fracture network, no faults dip at unfavorable angles out of the slope. For additional information and full details, the reader is referred to Willenberg (2004) and Willenberg et al. (2008a).

A new 3D tomographic seismic refraction technique was developed to determine the P-wave velocity structure of the unstable and adjacent parts of the rockslide (Figure 4). Inversion of first-arrival travel time picks revealed a broad zone of remarkably low seismic velocities (less than 1500 m/s). This ultra-low velocity zone extended to a depth of at least 25 m over a 200 x 100 m area significantly beyond the limits of the rock mass that is known to be currently moving. To explain such low velocities requires 17% of the investigated volume to be air-filled voids. Several faults transect the ultra-low velocity region, the trend of which paralleled part of the scarp generated by the 1991 rockslide events. Ubiquitous dry cracks, fracture zones, and faults are the likely cause of the anomalously low velocities. For full details and further information, the reader is referred to Heincke (2005) and Heincke et al. (2006a).

Borehole geo-radar experiments involved single-hole reflection surveys using a 100 MHz antenna system (Figure 5). Several hyperbolic reflections measured in three deep boreholes could be associated with planar fractures. Using velocity values obtained from a cross-hole experiment, the reflection travel times corresponding to the major fractures delineated in the televiewer log were predicted. Six out of the twenty predictions could be associated with hyperbolic reflection patterns observed in the geo-radar section. In addition, it was found that an important feature of the geo-radar data is the capability to determine the minimal extension of the major faults from hyperbolic reflection patterns. Applying basic migration principles to pattern end points, minimum extensions between 7.8 and 49 m were determined. For full details and further information, the reader is referred to Heincke et al. (2006b) and Spillmann et al. (2007b).

The cumulative results of this integrated geological / geophysical characterization of the 3D rock mass structure at Randa is thoroughly reported by Willenberg, 2004 and Willenberg, 2008a, and the reader is referred to these manuscripts for more detailed information. A cross-section through the geological model of the unstable rock mass, showing interpreted kinematic modes of failure and displacement rates derived from the most recent investigations, is shown in Figure 6.

### **Laboratory testing**

Intact rock strength properties of the augengneiss and the fine-grained chloritic and striped (para)gneisses (see Figure 3) were determined through laboratory testing (Willenberg, 2004). Samples were retrieved from coring of shallow boreholes (90 mm diameter, up to 5 m deep), and subject to both uniaxial and triaxial compression tests. Analysis of the recorded stress-strain curves provided the elastic constants, Young's Modulus (E) and Poisson's ratio ( $\nu$ ), the uniaxial compressive strength (UCS), and the Coulomb shear strength parameters, friction angle ( $\phi$ ) and cohesion (c) of the intact rock. Rock densities were also determined. Table 1 summarizes the measured intact rock strength properties for the two different materials found at Randa (Willenberg, 2004).

**Table 1:** Summary of intact rock strength properties.

	Young's modulus (GPa)	Poisson's ratio	UCS (MPa)	Friction angle (°)	Cohesion (MPa)	Density (kg/m <sup>3</sup> )
Augengneiss	32	0.21	97	55	16	2640
Paragneiss	21	0.14	69	32	19	2700

### Randa borehole sb120

Three deep boreholes were drilled at Randa during creation of the in-situ laboratory. Two boreholes penetrate to 50 m depth (sb50s and sb50n) while the third reaches a depth of 120 m (sb120). Figure 7 shows a layout of the three boreholes within the unstable rock mass. Each borehole is equipped with monitoring casing for periodic inclinometer surveys, piezometers and geophones encased in grout at the hole bottom, and each was logged with a borehole televiewer shortly after drilling. Borehole sb120 is also fitted with external brass rings at regular intervals for extensometer surveying using the INCREX system. Borehole sb120 (Figure 8) was chosen as the site to receive COGEAR instrumentation based on its ideal location within the unstable rock mass, the breadth and quality of information available, and the long existing time series of measurements.

Periodic inclinometer surveys were performed twice per year from 2002 through 2006, and more sparsely thereafter. All inclinometer surveys used a 61 cm base length, bi-axial instrument. Results for borehole sb120 are presented in Figure 9, and have been used to identify actively deforming faults along the borehole axis, and characterize their rates of displacement. Extensometer surveys using the INCREX system were performed in conjunction with inclinometer measurements twice per year. The sensor base length (and measurement interval) was 60 cm. Results are shown in Figure 9, and are again used to help characterize active faults and their axial displacement rates. Two in-place inclinometers were installed across discontinuities at 68 m and 85 m depth in borehole sb120. Their purpose was to monitor continuous deformations across these selected discontinuities and to detect any temporal changes in the displacement rate. The locations were chosen according to periodic inclinometer surveys, which showed significant displacement across the chosen faults. The in-place inclinometers were operational between January 2004 and August 2008, and were then upgraded with new fiber optic instruments (described below). Detailed description of these measurement systems and a full discussion of the results can be found in Willenberg (2004) and Willenberg et al. (2008a,b).

The traces of major fractures revealed with televiewer imaging in borehole sb120 are shown together with their resolved orientations in Figure 9. These fractures have widths greater than 2 mm and tend to contain intensely foliated material. The fractures are shown with the horizontal and axial displacement profiles derived from inclinometer and extensometer surveys, and the magnitude of the derived 3D displacement vector is also noted (for explanation of the analysis procedure see Willenberg, 2004). Results suggest that deformation is highly localized along certain identified faults. Regions of high fracture density (i.e. more than 3 fractures per 0.61 m) generally do not exhibit distributed displacement. Thus, internal deformation of the rock mass is accommodated primarily by dislocation of the active major faults. In Figure 10, the same fracture image and orientation data are shown together with summary results from borehole geo-radar surveying. Fractures are grouped into sets where possible. Correlations between geo-

radar reflections and televiwer imaging are apparent, and the most important reflections are highlighted and labeled.

For further information and all relevant data regarding borehole sb120, the reader is referred to Willenberg (2004) and Willenberg et al. (2008a,b).

### **COGEAR instrumentation installed in borehole sb120**

In order to capture the effects of passing seismic waves on induced deformations within the unstable rock mass at Randa, a monitoring system is required that can resolve very small displacements at appreciable sampling rates. The only monitoring instruments able to deliver such performance are fiber optic (FO) strain systems. Therefore, in order to extend our monitoring strategy into the dynamic regime within the framework of COGEAR, we installed a fiber optic monitoring system in borehole sb120 based on long-gage fiber Bragg grating (FBG) strain sensors.

Fiber Bragg gratings are short sections of optical fiber that contain a periodic variation in the index of refraction. When illuminated by broadband light, each FBG reflects a particular wavelength while transmitting all others undisturbed. In this way, multiple sensors can be placed in series on the same optical fiber, tuned at non-intersecting wavelength bands. The reflected wavelength is measured by an optical interrogator, and changes proportionally with the FBG strain within a linear regime. Advantages of fiber Bragg grating systems include high resolution, fast sampling rate, long sensor base lengths, insensitivity to electrical disturbances, robust cabling, and the possibility to chain many sensors together on a few cables.

The new monitoring package gives us micro-strain resolution and the capability to detect sub-micrometer scale deformations in both triggered-dynamic and continuous measurements. Dynamic measurements are triggered by sensor deformation and recorded at 100 Hz, while continuous measurements are logged every 5 minutes (the average of all readings over this time period). Two types of sensors have been installed: (1) fully-embedded borehole sensors in sb120, encased in grout at depths of 38, 40 and 68 m, and (2) crackmeters (crack extensometers) spanning active tension cracks on the ground surface. Borehole sb120 sensors were installed to span active faults showing normal mode offset (associated with block toppling), previously identified with inclinometer, extensometer, and borehole televiwer observations (Figure 11). Three 1.5 m baselength sensors make up one chain, and there are two identical chains (for redundancy). The sensors are fully embedded in grout that extends up to 20 m depth in the borehole. The new fiber optic crackmeters are 0.8 m in length and have both strain and temperature sensors so the strain record can be temperature compensated.

Full system specifications and detailed discussion of first monitoring results can be found in Moore et al. (2010). Relevant results from borehole sb120 are briefly reproduced here. Since installation, the FO monitoring system has been operational more than 90% of the time. Figure 12 shows the time series of measured displacements from the three different monitoring intervals in borehole sb120. All sensors are shortening as expected. Accelerated shortening following installation of the borehole sensors can be clearly observed during the first 2-3 months, and is related to long-term drying shrinkage of the grout. Otherwise, the sensors show deformation rates consistent with previous extensometer surveys (Figure 13). A number of transient signals (brief steps or drops) have been observed, which in some cases were large enough to trigger rapid sampling. The combination of short- and long-term observation offers relevant new insight into the deformation process, as shown for example in Figure 14.

The new FO monitoring system is well poised to make exciting and unique new measurements during an earthquake, and should reveal strong insights into the rockslide's seismic performance.

## References

- Eberhardt, E., Stead, D. & Coggan, J. (2004). Numerical analysis of initiation and progressive failure in natural rock slopes – the 1991 Randa rockslide, *International Journal of Rock Mechanics and Mining Sciences*, 41(1), 69-87.
- Gischig, V., Loew, S., Kos, A., Moore, J.R., Raetzo, H., and Lemy, F. (2009). Identification of active release planes using ground-based differential InSAR at the Randa rock slope instability, Switzerland, *Natural Hazards and Earth System Sciences* 9(6), 2027-2038.
- Heincke, B. (2005). Determination of 3-D fracture distribution on an unstable mountain slope using georadar and tomographic seismic refraction techniques. D.Sc. Thesis, Institute of Geophysics, ETH Zurich, Switzerland.
- Heincke, B., Maurer, H., Green, A.G., Willenberg, H., Spillmann, T. & Burlini, L. (2006a). Characterizing an unstable mountain slope using shallow 2- and 3-D seismic tomography. *Geophysics*, 71(6), B241-B256.
- Heincke, B., Green, A.G., Van Der Kruk, J., and Willenberg, H. (2006b). Semblance-based topographic migration (SBTM): a method for identifying fracture zones in 3D georadar data. *Near Surface Geophysics* 4, 79-88.
- Heynen, M. (2010). The influence of topographic amplification and local site conditions on the seismic stability of rock slopes (Seetalhorn, VS). Upcoming MSc Thesis, Engineering Geology, ETH Zurich, Switzerland.
- Loew, S., Willenberg, H., Spillmann, T., Heincke, B., Maurer, H., Eberhardt, E., and Evans, K. (2007). Structure and kinematics of a large complex rockslide as determined from integrated geological and geophysical investigations (Randa, Switzerland). *Proceedings 1st Int. North American Landslide Conference*, Vail, CO.
- Moore, J.R., Gischig, V., Button, E., and Loew, S. (2010). Rockslide deformation monitoring with fiber optic strain sensors, *Natural Hazards and Earth System Sciences* 10(2), 191-201.
- Sartori, M., Baillifard, F., Jaboyedoff, M. & Rouiller J.-D. (2003). Kinematics of the 1991 Randa rockslides (Valais, Switzerland). *Natural Hazards and Earth System Sciences*, 3, 423-433.
- Schindler, C., Cuenod, Y., Eisenlohr, T., & Joris, C.-L. (1993). Die Ereignisse vom 18. April und 9. Mai 1991 bei Randa (VS) - ein atypischer Bergsturz in Raten. *Eclogae geol. Helv.*, 86/3, 643-665.
- Spillmann, T., Maurer, H., Green, A.G., Heincke, B., Willenberg, H., and Husen, S. (2007a). Microseismic investigation of an unstable mountain slope in the Swiss Alps. *Journal of Geophysical Research* 112(B7).
- Spillmann, T., Maurer, H., Willenberg, H., Evans, K. Heincke, B., and Green, A.G. (2007b). Characterization of an unstable rock mass based on borehole logs and diverse borehole radar data. *Journal of Applied Geophysics* 61(1), 16-38.
- Willenberg, H. (2004). Geologic and kinematic model of a complex landslide in crystalline rock (Randa, Switzerland). D.Sc. Thesis, Engineering Geology, ETH Zurich, Switzerland.
- Willenberg, H., Loew, S., Eberhardt, E., Evans, K., Spillmann, T., Heincke, B., Maurer, H-R. & Green, A. (2008a). Internal structure and deformation of an unstable crystalline rock mass above Randa (Switzerland): Part I – Internal structure from integrated geological and geophysical investigations, *Engineering Geology*, 101, 1-14
- Willenberg, H., Evans, K.F., Eberhardt, E., Spillmann, T., and Loew, S. (2008b). Internal structure and deformation of an unstable crystalline rock mass above Randa (Switzerland): Part II – Three-dimensional deformation patterns, *Engineering Geology*, 101, 15-32



**Figure 1:** Overview of the Randa rockslide deposit in the Matter Valley.



**Figure 2:** Detail of the scarp and deposit of the 1991 failures at Randa.

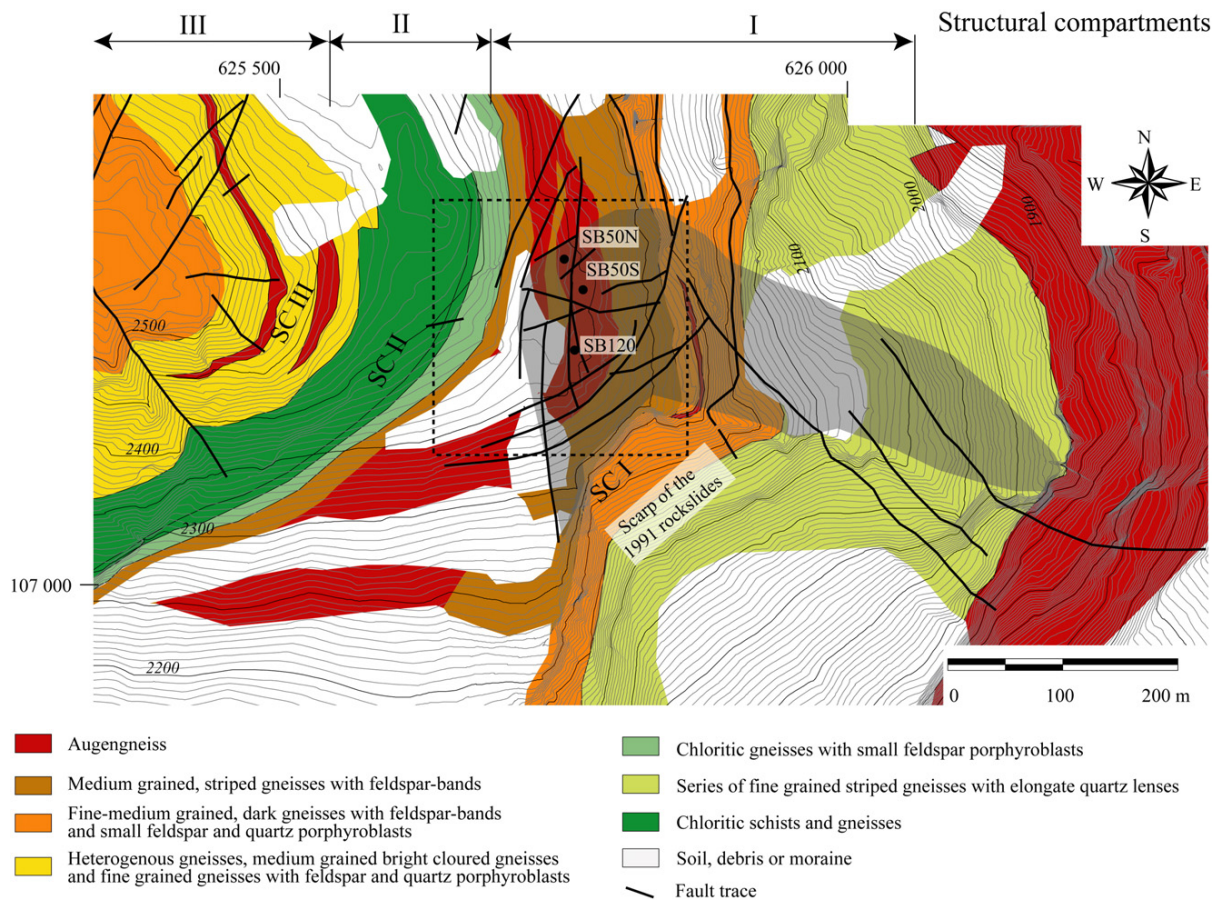


**Figure 3:** Geological and structural map of the area above and behind the scarp of the 1991 rockslides. Traces of surface faults and fracture zones are shown. Figure reproduced from Willenberg et al. (2008a).

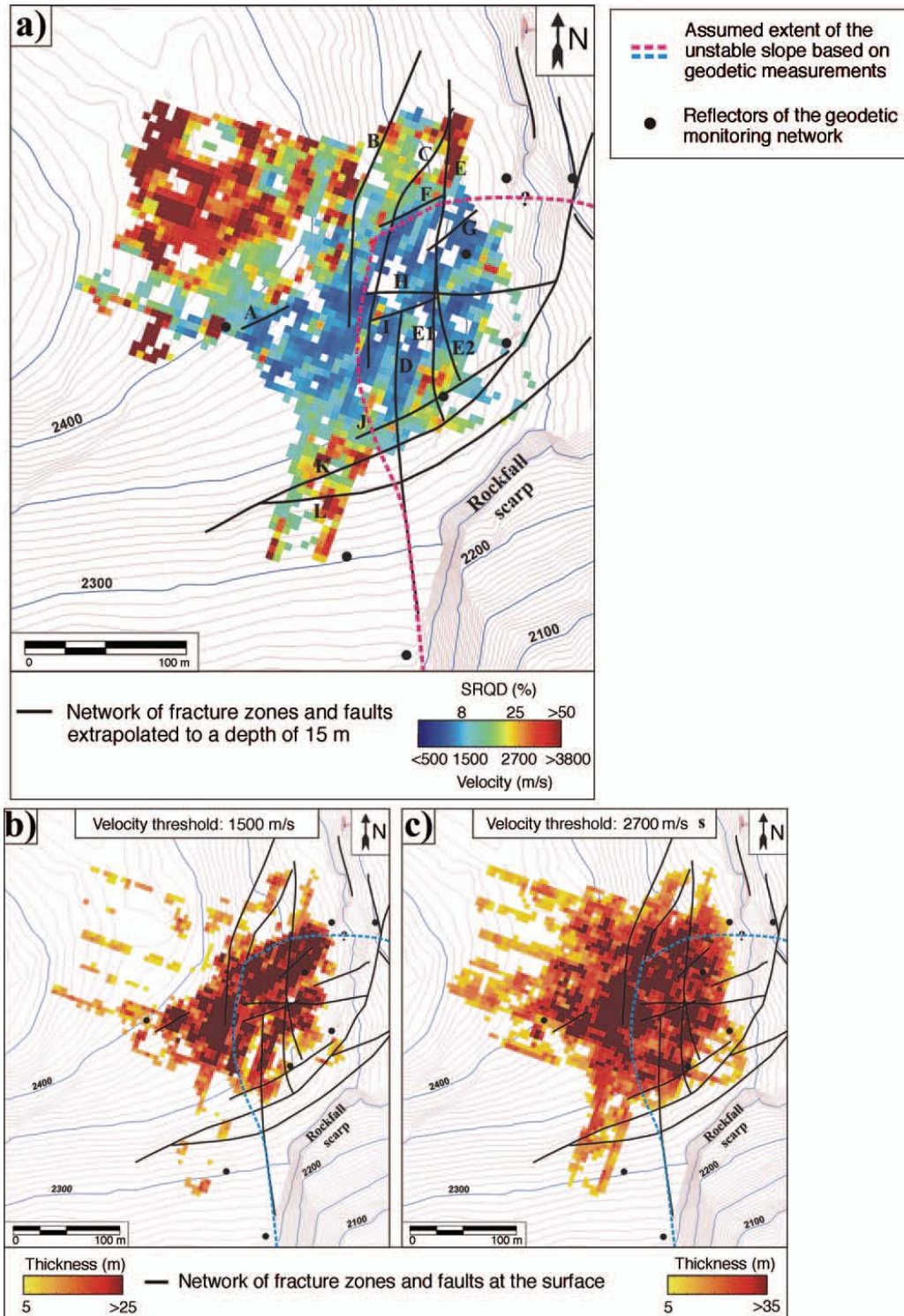


**Figure 4:** (a) P-wave velocity distribution determined from 3D seismic refraction tomography; (b) and (c) thickness of different low-velocity zones. Figure reproduced from Heincke et al. (2006a).

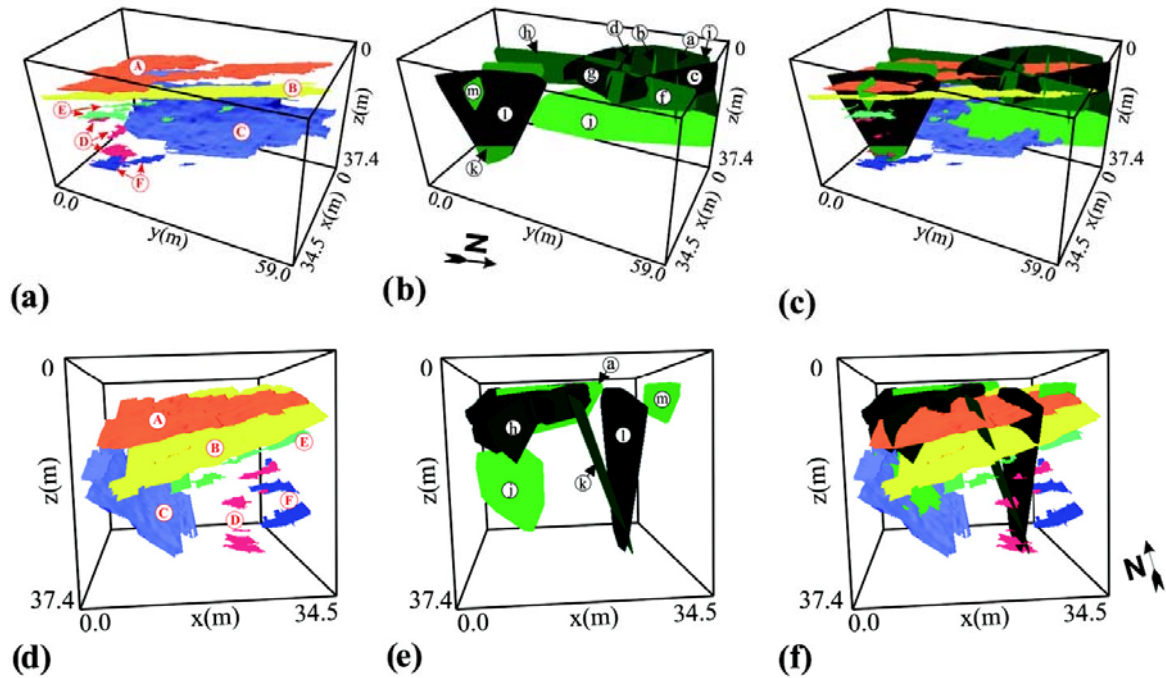


**Figure 5:** Results of 3D geo-radar surveying used to identify planar surfaces representing different faults and fracture zones. Parts (c) and (f) are the combination of information in (a) and (b), and (d) and (e), respectively. Figure reproduced from Heincke et al., 2006b).

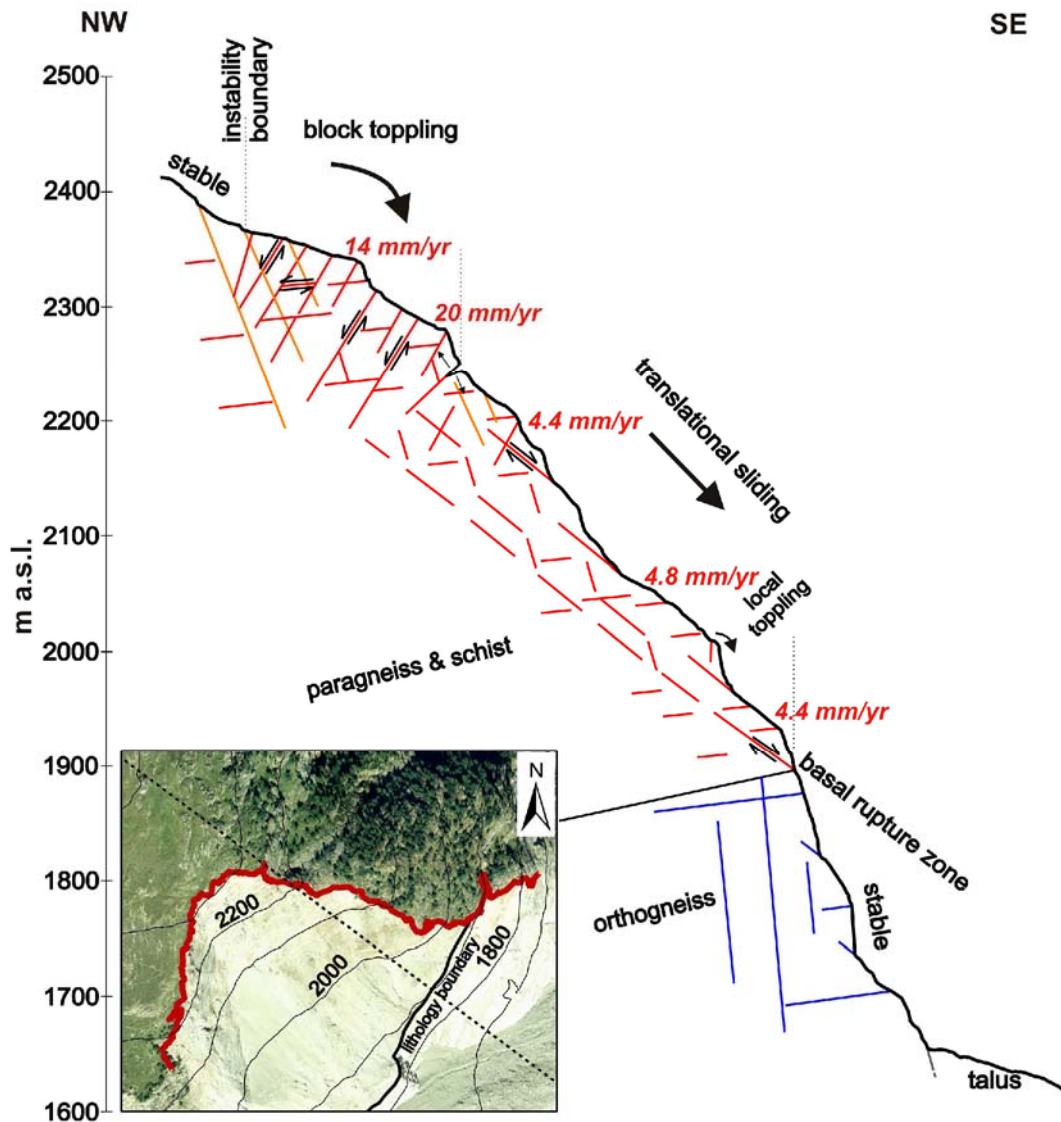


**Figure 6:** Cross-section through the currently unstable rock mass at Randa showing Conceptual 2-D kinematic model of the instability. Block toppling observed in the upper part of the instability changes to translation sliding in lower areas, and a basal rupture surface can be definitively observed. Figure reproduced from Gischig et al. (2009). Velocities indicated are the displacement rates derived from GB-DInSAR.

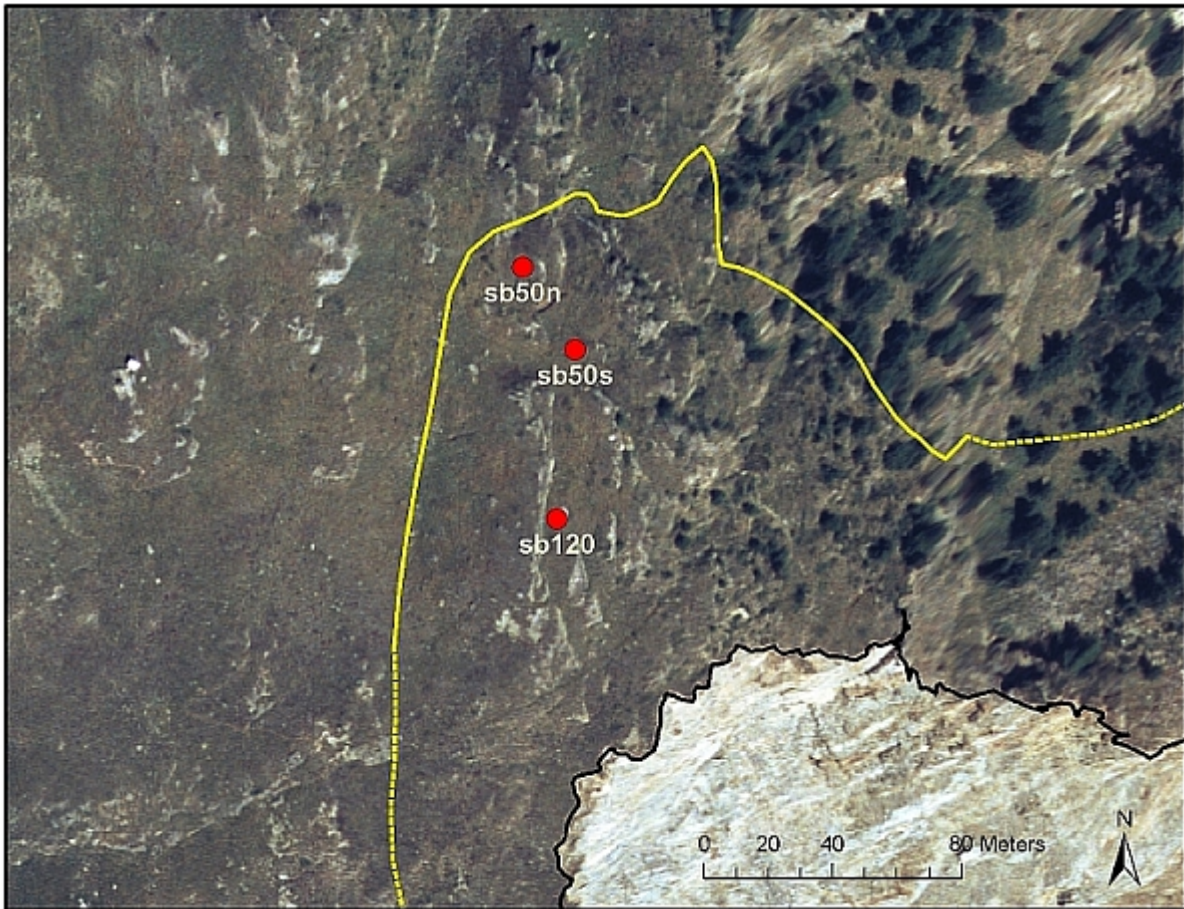


**Figure 7:** Overview of the three deep boreholes at the Randa in-situ laboratory. The number in the name indicates the borehole depth. Yellow line shows the suspected boundary of the current instability.



**Figure 8:** Borehole sb120 at Randa, showing the surrounding area and borehole top, and detail of the inclinometer casing and in-place inclinometer instrument.

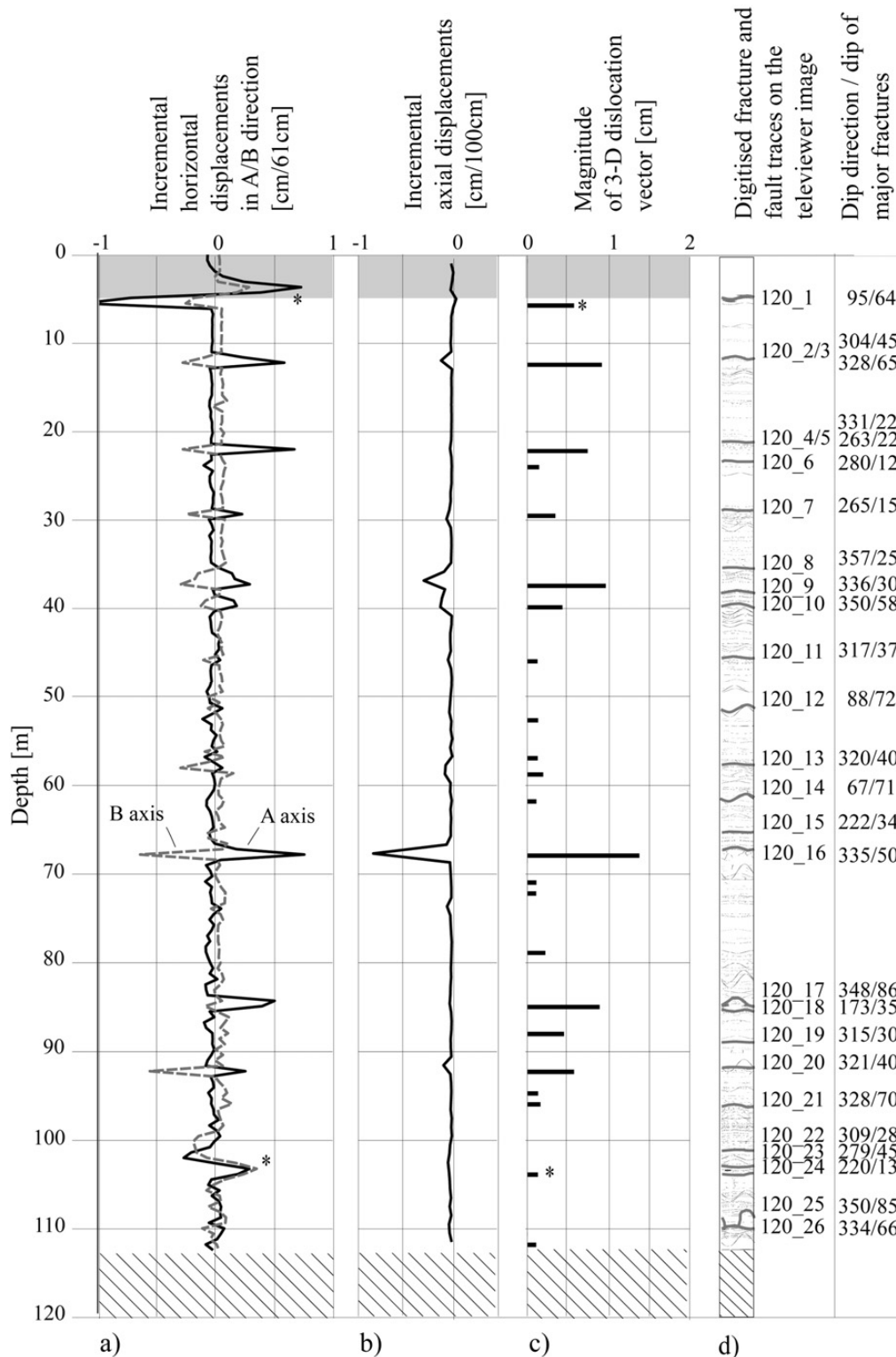


**Figure 9:** Summary of inclinometer, extensometer, and televiewer results for borehole sb120. Horizontal and axial displacements along the identified fault zones are shown, as well as the 3D magnitude and structure orientation. Figure reproduced from Willenberg et al. (2008b).

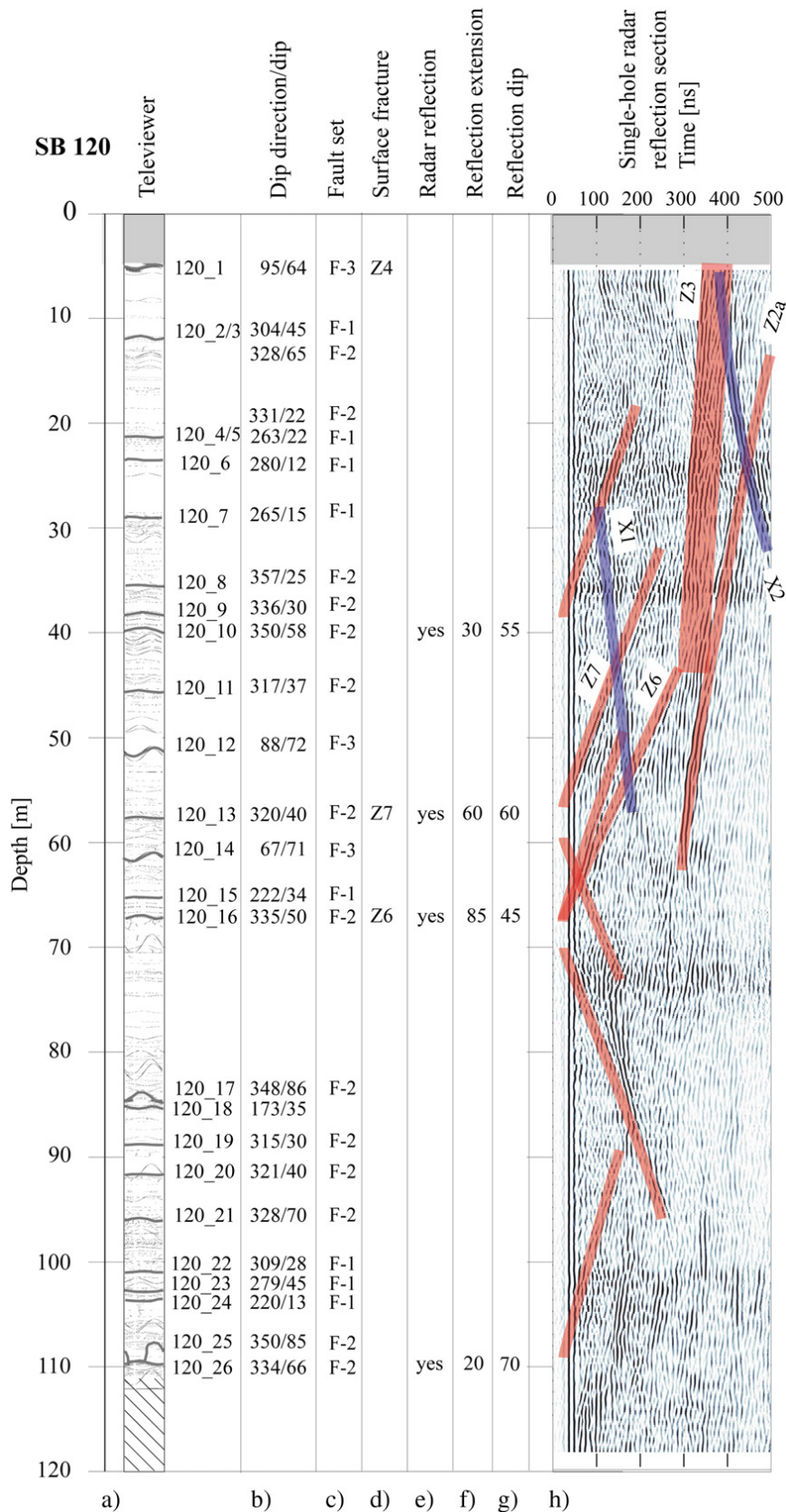


**Figure 10:** Comparison of borehole televiewer mapping and borehole fracture surveys with borehole geo-radar data. The orientations of labeled fractures are shown, as well as their respective fault set association. Figure reproduced from Willenberg et al. (2008a).

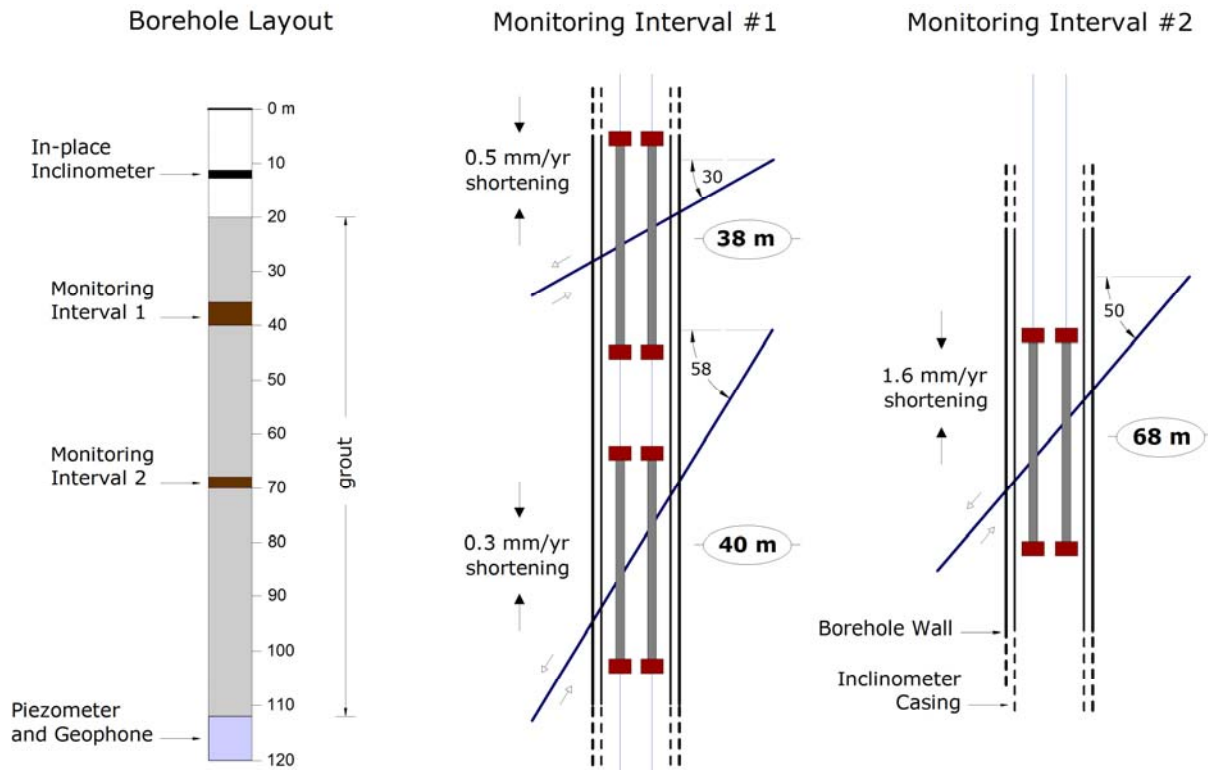


**Figure 11:** Detail of fiber optic sensor installation in borehole sb120. Two monitoring intervals were selected to span three active faults showing normal mode offset (see slip arrows). The expected rates of shortening, calculated from previous extensometer surveys, are shown. Two active parallel sensor chains were installed for redundancy and security, and a third inactive chain (not shown) acts as reserve. Figure reproduced from Moore et al. (2010).

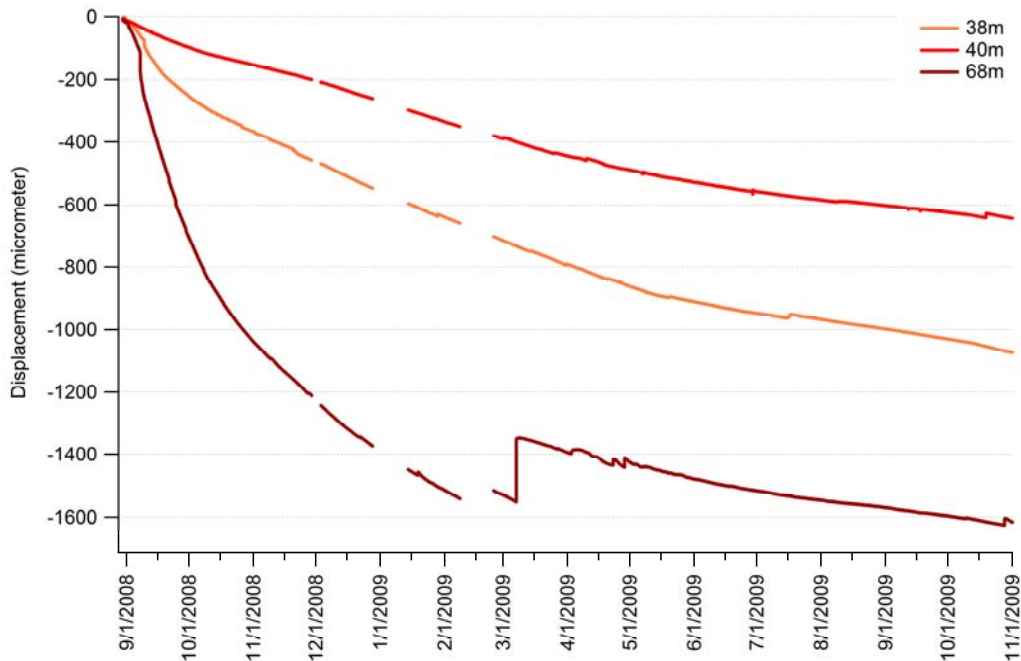


**Figure 12:** Deformation time series measurements from the three sensors at different monitoring intervals in borehole sb120. All sensors are shortening as expected. Accelerated shortening is seen immediately following sensor installation, which likely results from shrinkage of the grout. A number of transient steps and drops occur throughout the time history; one event from April 28, 2009 is highlighted in the following Figure. Dates are m/d/y. Figure reproduced from Moore et al. (2010).

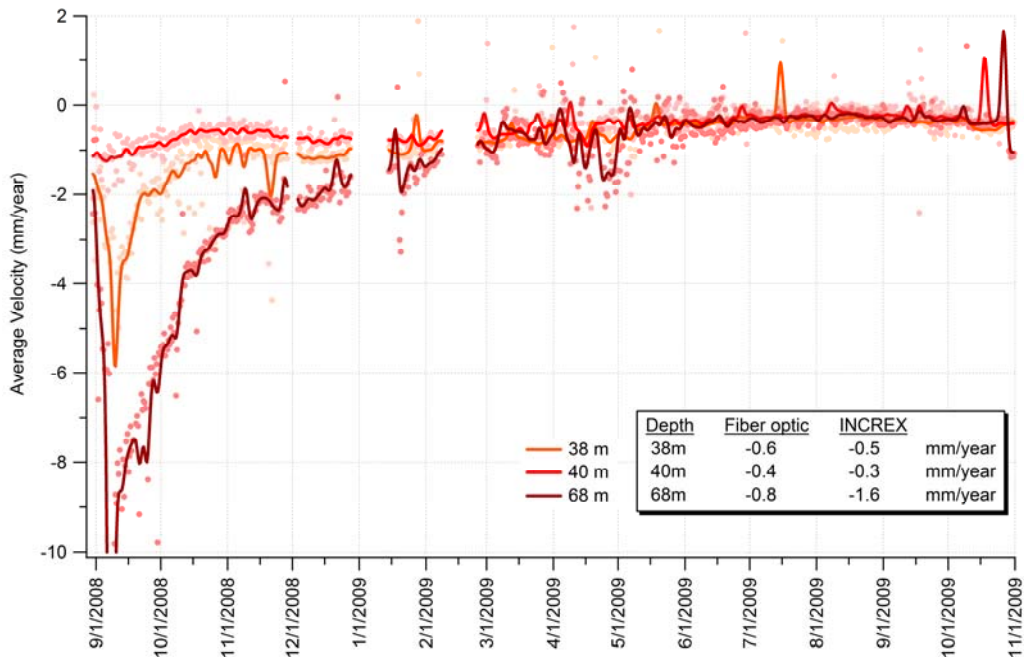


**Figure 13:** Velocity time series for the different sensors in borehole sb120. The inset table shows comparison of the long-term average velocities with those determined from previous INCREX extensometer surveys. Accelerated shortening is clearly visible in the first 2-3 months of operation. Dates are m/d/y. Figure from Moore et al. (2010).

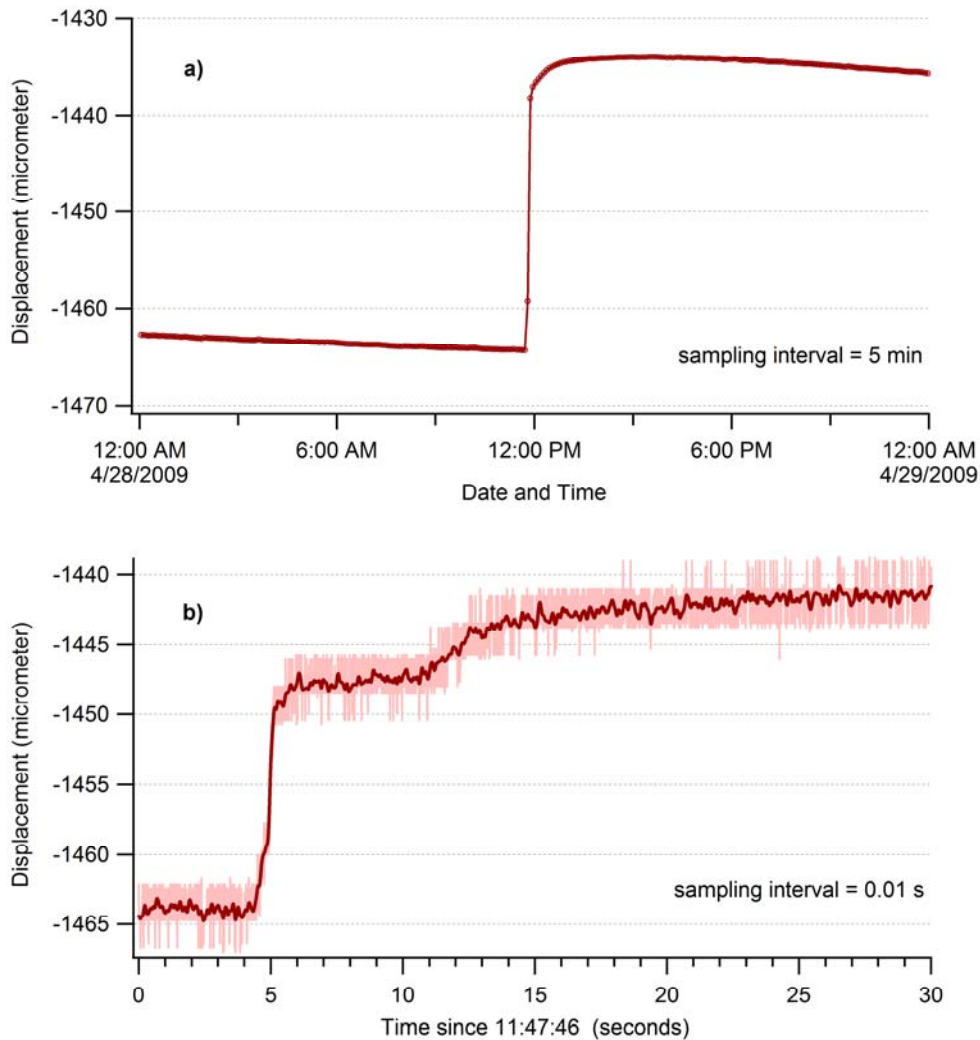


**Figure 14:** a) Expanded view of the transient step occurring on April 28, 2009. The event was a rapid period of axial extension amounting to about  $30 \mu\text{m}$  at the deepest sensor (68 m), contrasting to otherwise steady shortening (see Figure 3). b) The step was large enough to also trigger rapid 100 Hz sampling. Observed details indicate that the majority of deformation occurred through one large step lasting roughly 1 s, and that deformation continued with a smaller, slower step followed by slow continuous extension. Figure reproduced from Moore et al. (2010).